BNL-222579-2022-JAAM

A full-ring variable-aperture cadmium zinc telluride system for whole-body single photon emission computed tomography: realistic simulations with phantoms

Y. Huh, Y. Cui

To be published in "Medical Physics"

January 2022

Nonproliferation and National Security Department

Brookhaven National Laboratory

U.S. Department of Energy

National Institute of Health

DISCLAIMER

A full-ring variable-aperture cadmium zinc telluride system for whole-body single photon emission computed tomography: realistic simulations with phantoms

Yoonsuk Huh[1*], Javier Caravaca[1*], Jaehyuk Kim[2], Yonggang Cui[3], Qiu Huang[4], Grant Gullberg[1,5], and Youngho Seo[1,5,6,7,8]

[1]Department of Radiology and Biomedical Imaging, University of California, San Francisco, CA, USA

[2]Princess Margaret Cancer Centre, University Health Network, Toronto, ON, Canada

[3]Department of Nonproliferation and National Security, Brookhaven National Laboratory, Upton, NY, USA

[4]Department of Nuclear Medicine, Ruijin Hospital, School of Biomedical Engineering, Shanghai Jiao Tong University, Shanghai, China

[5]Molecular Biophysics and Integrated Bioimaging Division, Lawrence Berkeley National Laboratory, Berkeley, CA, USA

[6]Department of Radiation Oncology, University of California, San Francisco, CA, USA

[7]Joint Graduate Group in Bioengineering, University of California, San Francisco and Berkeley, CA, USA

[8]Department of Nuclear Engineering, University of California, Berkeley, CA, USA

[*]Co-first authors

Corresponding authors contact:

UCSF Physics Research Laboratory

Department of Radiology and Biomedical Imaging
University of California, San Francisco, California, 94143-0946
Emails: javier.caravacarodriguez@ucsf.edu, youngho.seo@ucsf.edu
Phone: (415) 353-9464

Abstract

Background

Single photon emission computed tomography (SPECT) is an imaging modality that has demonstrated its utility in a number of clinical indications. Despite this progress, a high sensitivity, high spatial resolution, multi-tracer SPECT with a large field of view suitable for whole-body imaging of a broad range of radiotracers for theranostics is not available.

Purpose

We have designed a cadmium zinc telluride (CZT) variable-aperture full-ring SPECT scanner instrumented with a broad-energy tungsten collimator intended to fill this technological gap. The final purpose is to provide a multi-tracer solution for brain and whole-body imaging. Our static SPECT scanner breaks the paradigm of the standard dual- and triple-head rotational SPECT systems, utilizing a larger detector area in each scan increasing the sensitivity. We provide a demonstration of the performance of our design using a realistic model of our detector with simulated body-sized ^{99m}Tc phantoms.

Methods

We developed a realistic model of our detector by using a combination of a Geant4 Monte Carlo simulation and a CZT detector response model based on a finite element model. Our approach models the characteristic low-energy tail effect in CZT that noticeably affects the sensitivity and the quality of the scatter correction in CZT detectors. We implement a modified dual energy window scatter correction adapted to include the CZT low-energy tail effect. A dedicated correction is also developed to eliminate the undesirable truncation observed in images given the presence of detector edges and gaps between detectors, due to the non-rotational nature of our device. Corrections for the attenuation, detector response

and the presence of collimators are also included. The images are reconstructed using the maximum-likelihood expectation-maximization algorithm implemented in the reconstruction open software STIR. Detector and reconstruction performance are characterized with a Derenzo phantom and a body-sized National Electrical Manufacturers Association (NEMA) Image Quality (IQ) phantom containing ^{99m}Tc.

Results

Our SPECT design can resolve 6.4mm rods in a Derenzo phantom and obtain a good image contrast with the IQ phantom. Explicit testing of the gap and edge correction is provided, showing an excellent performance in eliminating the image truncation artifacts. Our modified scatter correction shows no overestimation of the contrast-recovery ratio for our realistic CZT detector model, as opposed to the cases without correction and with a standard dual-energy window scatter correction.

Conclusions

In this paper, we further demonstrate the performance of our design for whole-body imaging purposes. This adds to our previous demonstration of improved qualitative and quantitative ^{99m}Tc imaging for brain perfusion and ^{123}I imaging for dopamine transport with respect to state-of-the-art NaI dual-head cameras. We show that our design performs similarly to the VERITON SPECT from Spectrum Dynamics, a commercial full-ring CZT SPECT camera, with the potential advantage of the broader energy range of application given by our custom-design tungsten collimators. Our device combines high sensitivity and image resolution with a broad-energy imaging application for the purpose of clinical imaging and theranostics of emerging radionuclides.

Keywords

SPECT, CZT, full-ring, Monte Carlo simulation, finite element method

1. Introduction

Single photon emission computed tomography (SPECT) is a very important imaging modality in nuclear medicine, including cardiac imaging [1]. SPECT systems keep continuously evolving with the goal of improving sensitivity, spatial resolution, image quality, and to access to a larger number of radionuclides by broadening the gamma ray energy application range.

One of the most recent technological breakthroughs is the implementation of the semiconductor cadmium zinc telluride (CZT) in SPECT systems [1], providing higher energy resolution, a reduced detector size, and a lighter weight than that compared to the combination of photomultiplier tubes and scintillation crystals [2-4]. Another important advance is the substitution of the standard dual- or triple-head SPECT rotating around the subject, by a semi-stationary and multi-headed ring geometry in which each head independently moves forward and backward to get very close to the subject, with an additional swiveling motion to allow them to face the subject and reduce the number of unused detector parts to a negligible fraction [5].

In [6], we proposed a variable-aperture full-ring CZT SPECT system with the addition of custom-designed multi-energy tungsten collimators, with an application energy range of 100keV to 250keV [7], that could provide a multi-tracer imaging solution with excellent sensitivity and image quality. Targeting the imaging of ^{99m}Tc-based brain perfusion [8] and ^{123}I-based dopamine transporter [9], we showed a reduced acquisition time and improved sensitivity with equivalent contrast-to-noise ratio (CNR) and spatial resolution compared to conventional two-headed NaI-based SPECT systems.

In this paper, we further explore our design by evaluating it for whole-body imaging purposes employing a Derenzo hot rod phantom and a National Electrical Manufacturers Association (NEMA) Image Quality (IQ) phantom. Furthermore, we improve our detector simulation by including a realistic CZT response based on a finite element method (FEM) model [10], and we improve the obtained images by adding an energy-window-based scatter correction [11].

Section 2 describes the detector geometry, Monte Carlo simulation, FEM model, image reconstruction strategy and scatter correction. **Section 3** shows the predicted performance of our system with the phantoms, **Section 4** discusses the results and **Section 5** provides the summary and conclusion.

2. Materials and methods

In this section we describe the detector's design, our Monte Carlo simulation, including the FEM model, and present our image reconstruction approach, including generation of the projections and application of the scatter correction (see **Fig. 1** for an overview of the analysis flow).

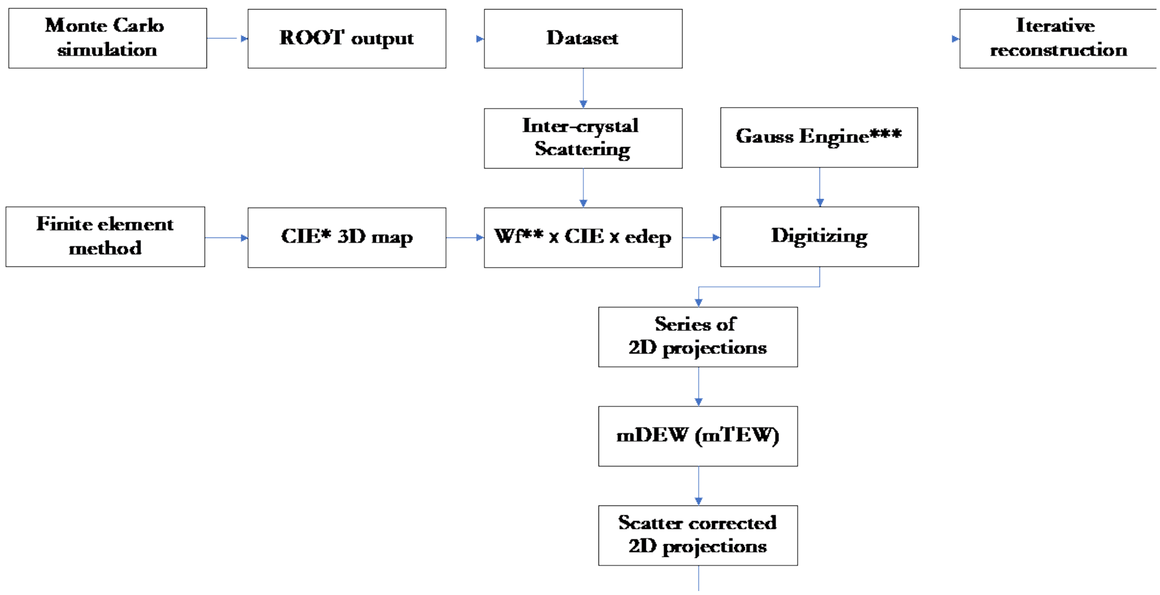

Figure 1. Diagram summary of our approach. The GEANT4 MC simulation and the FEM model are used to produce the SPECT projections that are further scatter-corrected and finally reconstructed to yield the final tomographic image of the phantoms.

*Charge induction efficiency. **Weighting factor. ***Referenced from Geant4 and GATE codes

2.1 System and phantom geometries

Our design is composed by eight independently movable and swiveling detector heads arranged in a full-ring configuration [6]. Each head has a 179.2 mm × 128 mm detector surface with 1.6 mm × 1.6 mm × 5.0 mm pixel size, and swivels in 5° steps from -42.5° to 42.5° (18 steps total). The detector heads are located at 240 mm radius around the center of the imaging region (**Fig. 2a**), further than in our previous brain imaging experiment [6]. Given the further distance, the heads are rotated 90° around their perpendicular axis so that the shorter side of the head is parallel to the axial direction in order to cover a larger angular region. **Table I** summarizes our system specifications. The geometries of the phantoms are shown in **Fig. 2b, c**.

Table I. Specifications of CZT-SPECT scanner for Monte Carlo Simulation

Parameter	Whole-body SPECT
Number of detector heads	8
Detector material	CZT
Detector head size	179.2 mm × 128 mm × 5.0 mm
Pixel pitch	1.6 mm × 1.6 mm
Collimator hole shape	Rectangular
Collimator material	Tungsten-Alloy
Collimator length	25 mm
Septal thickness	0.32 mm
Collimator hole size	1.28 mm
Detector heads radial position	240 mm
Range for rotation angle	-42.5° ~ 42.5°
Step angle	5°
Number of projections	72
Time exposure per step	20s

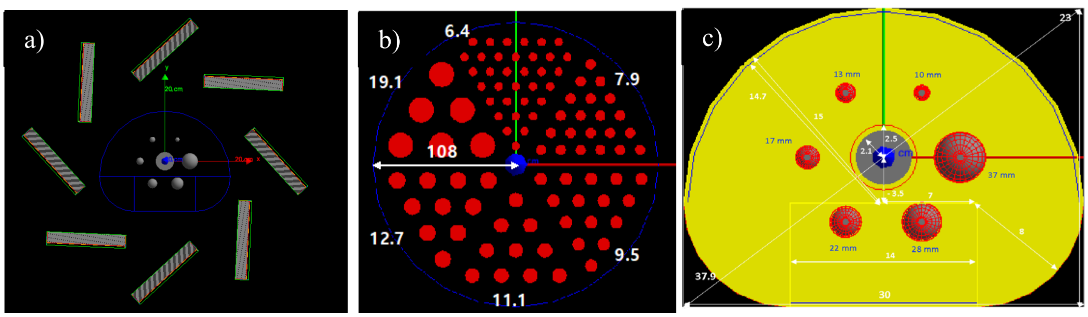

Figure 2. a) Front view of the system geometry in the GATE tool with the NEMA IQ phantom for scale. **b)** Derenzo hot rod phantom seen from the front with the rods marked in red and with the number corresponding to their diameters in millimeters. **c)** NEMA IQ phantom seen from the front. The spheres are highlighted in red and labeled by their diameters, and the warm background is in yellow.

2.2 Simulation model

Achieving an accurate detector simulation is crucial for the detector design phase. It has been shown that the charge transport, trapping and diffusion, affect the charge collection efficiency (CIE), charge sharing between pixels, and crosstalk in CZT. These effects introduce important features in the energy spectra, namely, a low-energy tail given by a fraction of photoelectric events, which reduces sensitivity, and a contamination of the photopeak energy window with scattered photons, which reduces image contrast and quantification accuracy [12-14]. Hence, the simulation of this effect is crucial for an accurate detector model. Models based on a FEM have been successfully developed and validated in [10, 12, 14], following the method suggested in [15, 16].

To simulate our detector, we follow an approach similar to the one in [10], in which a detector model based on GEANT4 Monte Carlo (MC) simulations and a COMSOL MULTIPHYSICS FEM implementation is adopted.

2.2.1 Monte Carlo simulation

We use the Geant4 Application for Tomographic Emission (GATE) [17] to simulate gamma ray propagation in the subject and detector. The particle transport is modelled by the emstandard_opt4 model, which uses the G4LivermorePhotoelectricMode and G4RayleighScattering Geant4 models that provide a high accuracy simulation of electrons and ion tracking. We added the RadioactiveDecay Geant4 process in order to model radionuclide gamma ray emissions.

The CZT material region is defined as sensitive detectors in Geant4 to store the information of the energy depositions. The tracking information of each photon is recorded in ROOT format indexed by run, event, detector and pixel, as well as the deposited energy values and their local positions in the pixel. Inter-crystal Compton scatter events were identified by hits generated in the same event but at different detector and pixel index numbers. An energy resolution of 6.5% full width at half maximum (FWHM) for CZT is simulated as a Gaussian smearing of the deposited energy value provided by GATE.

2.2.2 Finite element model

The number of generated charge carriers (electron and hole pairs) in CZT is proportional to the deposited energy. These carriers need to drift towards the anode or the cathode to be detected. This process is affected by the charge transport, trapping and diffusion [12], which yields a position-dependent charge induction efficiency (CIE) that need to be accounted for in order to obtain a realistic CZT detector response.

In [6] we approximated this effect by a simple inefficiency factor of 65%. For this study, we follow the more sophisticated method described in [10]. We estimate the CIE using the adjoint electron n* continuity equation suggested in [15, 16]

$$\frac{\partial n^*}{\partial t} = \mu_e \nabla\varphi \nabla\phi_w - \frac{n^*}{\tau_e} + \mu_e \nabla\varphi \nabla n^* + D_n \nabla^2 n^* \text{ , (1)}$$

where φ is the electric potential, μ_e is the mobility of the electrons, ϕ_w is the weighting potential, τ_e is the average lifetime of the electrons, and D_n is the diffusion constant for electrons. The value of φ can be obtained by solving the Laplace equation,

$$\nabla^2 \varphi = 0 \text{ . (2)}$$

Both holes and electrons are considered.

The charge transport model was implemented in the COMSOL MULTIPHYSICS software and equation (1) solved with the FEM model. We considered a 3 pixel × 3 pixel detector module with the same pixel size corresponding to our MC model. The required material property parameters were acquired from the specifications of the CZT detector M1085 from REDLEN (**Table II**).

Table II. Specifications of CZT material for finite element model

Material Properties	
Average atomic number	49.1
Density	5.78 g/cm^3
Electron mobility	1000 cm^2/V/s
Electron lifetime	3×10^{-6} (s)
Hole mobility	50 ~ 80 (cm^2/Vs)
Hole lifetime	10^{-6} (s)
Dielectric constant	10.9
Resistivity	3×10^{10} (cm)
Nominal bias voltage	-500V
Plating material (anode and cathode)	Au

Three 3D CIE maps were obtained by solving Eq. (1) for three-pixel positions: center, side and edge. **Fig. 3a** shows the CIE map for the center pixel. The CIE as a function of the depth of the gamma ray interaction in the pixel is shown in (**Fig. 3b**) compared to a bias voltage of -300V to show the dependency of CIE with this parameter. The curves are averaged over the X and Y dimensions. The small-pixel effect [18] is clearly observed in **Fig. 3b**, as well as the fact that a low bias voltage results in a lower and non-constant CIE for shallow detector depth, increasing the probability of populating the low-energy tail. **Figure 3c** shows the averaged CIE curves as a function of interaction depth for center, edge, and side pixels at the nominal -500V voltage. The CIE for edge and side pixels are lower and present a smoother trend than that of the center pixel. For simplicity and given the very small differences, we use the CIE obtained with the center pixel to model all the pixels in our detector. The CIE map obtained with the nominal bias (-500V) was exported to a text file for posterior use in the calculation of the deposited energies.

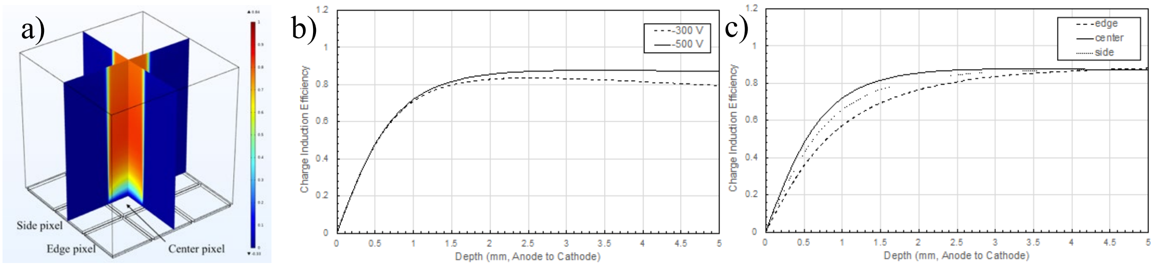

Figure 3. a) Central slice of the CIE map obtained from COMSOL for the central pixel. **b)** CIE as a function of interaction position depth for the center pixel obtained for -300V and -500V bias voltage. **c)** CIE as a function of interaction position depth for the center, edge, and side pixels. All the curves are averaged over the X and Y dimensions.

The total energy spectrum obtained for a ^{99m}Tc point source at the center of the detector with and without the CIE factor is shown in **Fig. 4**, where we observe that the CIE decreases the number of counts in the photopeak region by approximately 70% and increases the contribution of photoelectric events to the low-energy tail.

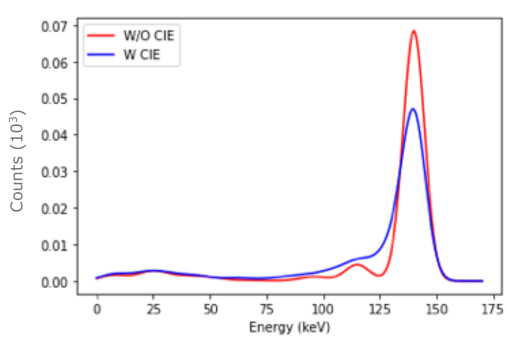

Figure 4. Energy spectra of a ^{99m}Tc point source in air with and without CIE.

2.3. Scatter correction and image reconstruction

Projections of two adjacent detector heads are conjoined to create extended projections that overcome the limited transaxial view, as detailed in our previous study [6]. These projections are corrected by the Compton scattering of gamma rays in the subject by using an energy window method [19]. A major consequence of the low-energy tail in CZT is that it complicates energy window-based scatter correction methods since the contamination of photopeak events in the low-energy tail leads to an overcorrection [20]. A standard dual-energy-window (DEW) scatter correction was successfully adapted for CZT by modeling the CZT low-energy tail with using data-driven approaches in [11, 20] and MC-driven approaches in [13, 21].

In this study, we compared two different DEW scatter correction methods: one with a typical DEW method (DEW) and another modified DEW that includes a low-energy tail correction for CZT (mDEW). The DEW method assumes that the number of scattered photons inside the photopeak window used for the projections can be estimated from the number of scattered photons in a lower energy window [19]. Then, for pixel j of a given projection

$$n_{PM}^{j} = n_{PE}^{j} + n_{S}^{j} = n_{PE}^{j} + k\, n_{SM}^{j}\ , \quad (3)$$

where n^{j}_{PM} is the total number of events measured in the photopeak window, n^{j}_{PE} is the number of photoelectric interactions in the photopeak window, n^{j}_{S} is the number of Compton interactions in the photopeak window, n^{j}_{SM} is the total number of events measured in a low-energy window, and k is a factor that needs to be modeled or determined empirically. We use the typical value $k = 0.5$ [19]. For DEW we consider a scatter window from 122 keV to 130 keV and a photopeak window from 131 keV to 149 keV.

The mDEW considers that the low-energy window is also populated by photoelectric interactions with a low CIE [11, 20], so Eq. (3) is modified to:

$$n_{PM}^{j} = n_{PE}^{j} + k_m(n_{SM}^{j} - m\, n_{PE}^{j}) \Rightarrow n_{PE}^{j} = n_{PM}^{j} - k_M(n_{SM}^{j} - m\, n_{PE}^{j})\,, \quad (5)$$

where m is the fraction of n^j_{PE} that ends up in the lower energy window. For mDEW we define a scatter window from 110 keV to 130 keV and a photopeak window from 131 keV to 149 keV.

We compute k_M and m by simulating a ^{99m}Tc point source in air, assuming that this environment is scatter free, and compare the given energy spectrum with the one obtained with the NEMA IQ phantom [11, 20]. **Figure 5** shows the energy spectra obtained with a ^{99m}Tc point source in air and with the NEMA IQ phantom with spheres of activity of 80 kBq/ml placed in a warm background of 10 kBq/ml of ^{99m}Tc. We estimate k_M and m to be 0.611 and 0.264, respectively.

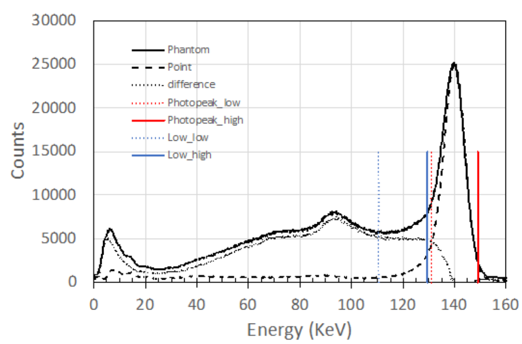

Figure 5. Energy spectra obtained with the ^{99m}Tc point source (dashed) and with the NEMA IQ phantom (solid) with CIE applied. These are used to calculate the parameters k_M and m for the mDEW scatter correction. The energy windows of mDEW are highlighted.

The series of 2D extended projections of 224 × 80 pixels was reconstructed using the maximum likelihood expectation maximization (MLEM) method [22] implemented in the software for tomographic image reconstruction (STIR) package [23, 24]. This package takes into account the scatter correction calculated above, and corrections for the gamma ray attenuation and the collimator and detector response, which were computed in our previous study [6]. The matrix and the pixel size of the reconstructed images are 224 × 224 × 80 with 1.6 mm pixel size, and the number of iterations for MLEM reconstructions was set to 40.

3. Results

In this section we evaluate the performance of our system with a Derenzo and a NEMA IQ phantom and estimate the spatial resolution and contrast recovery, comparing it with the literature.

3.1. Derenzo hot rod phantom

A Derenzo hot rod phantom, as shown in **Fig. 2b**, with a rod activity of 300 kBq/ml, is reconstructed using the method described in **Sec. 2**, resulting in the images shown in **Fig. 6**. The images do not include the collimator, detector response and scatter corrections, which their performance are discussed in the next section with the NEMA IQ phantom. The rod diameters are greater than the ones used in our previous brain study [6], given the larger size of the subject. To test the gap and edge correction methods developed in [6] and to show the effect of these corrections, we show in **Fig. 6** the reconstructed images with and without corrections and with only one of the corrections applied, along with the differences between the images. The fully corrected image of the hot rod phantom (**Fig. 6d**) shows no truncation artifacts despite some rods of the phantom being outside of the field of view (FOV) of our detector, due to our gap and edge corrections. Most of the 7.9mm rods and the top row of 6.4mm rods can be clearly resolved. The resolution is worse towards the center of the phantom. This is similar to the results obtained with the VERITON SPECT [5], where they could resolve the 6.4mm rods of the phantom , outperforming a dual-head NaI(Tl) camera (9.5mm rods).

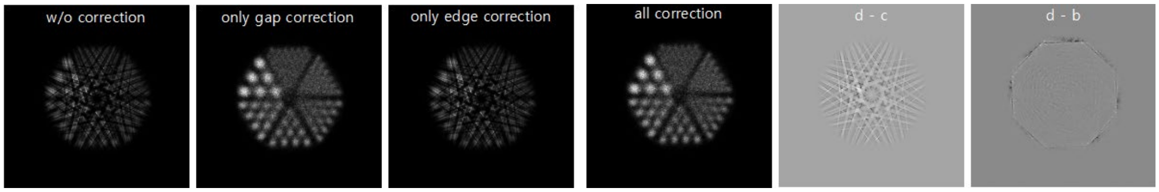

Figure 6. Axial reconstructed images of the hot-rod phantom with and without gap and edge corrections and difference between images. These images correspond to the projection of 55 slices with attenuation correction and without collimator, detector response or scatter corrections applied. **a)** without corrections, **b)** with gap correction, **c)** with edge correction, **d)** with both gap and edge corrections, **e)** difference between the fully-corrected and the gap-corrected images, **f)** difference between the fully-corrected and the edge-corrected images.

3.3. NEMA IQ phantom

A NEMA IQ phantom with 6 spheres of different sizes (**Fig. 2**) and activities of 80kBq/ml placed in a warm background of 10kBq/ml of ^{99m}Tc is reconstructed. **Figure 7** shows the reconstructed images of the NEMA IQ phantom images without scatter correction and with DEW and mDEW corrections. The images are normalized to the same value, the maximum pixel value of the three images, so that they can be directly compared with each other. No truncation artifacts are observed in the spheres or background. The application of mDEW results in slight increase of noise compared to the others due to the subtraction of true counts detected in the low-energy tail. The observed image contrast is equivalent to the one obtained by the VERITON CZT SPECT [5].

We quantitatively assess the image quality as recommended by the NEMA standard NU2-2007 for characterization of positron emission tomography (PET) scanners. We calculate the contrast recovery coefficient (CRC) for each of the six spheres as

$$CRC = \frac{M_{sphere}/M_{bg} - 1}{R_{sphere}/R_{bg} - 1} \quad (1)$$

where M_{sphere} and M_{bg} are the measured activities and R_{sphere} and R_{bg} are the true activity values inside the spheres and in the warm background, respectively. A comparison of the CRC values as a function of the sphere diameter without correction and with the DEW and mDEW corrections are in **Fig. 8**. We observe how in the absence of correction and with the typical DEW correction, the CRC values are overestimated, showing that mDEW provides a fast and simple scatter correction method for our case. This can be further refined by model-based correction methods to be used in multi-tracer scenarios.

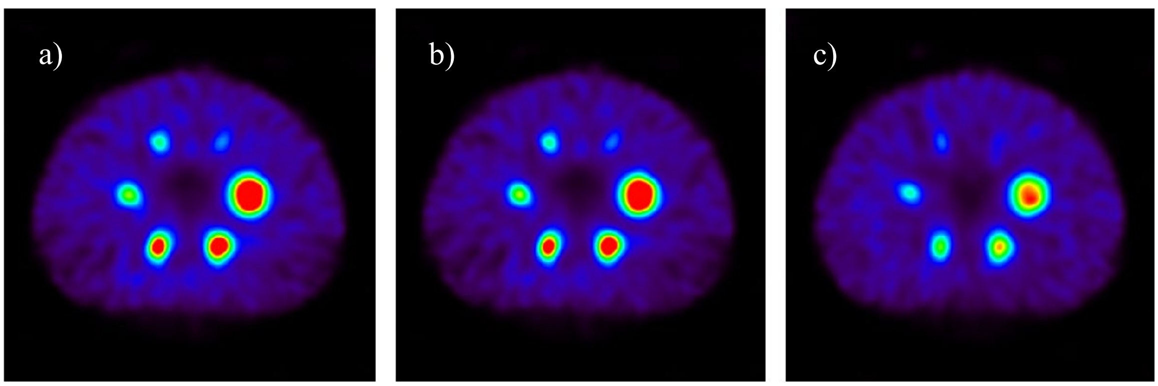

Figure 7. Reconstructed NEMA IQ phantom images without DEW scatter correction **(a)**, with typical DEW scatter correction **(b)**, and with modified DEW scatter correction **(c)**. All images were postprocessed using a 3D Gaussian filter with a sigma of 1 pixel.

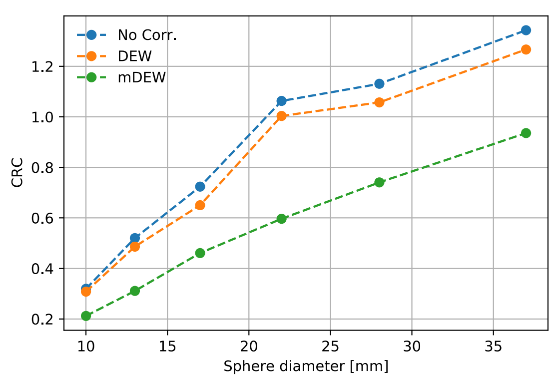

Figure 8. Contrast recovery coefficient without scatter correction, with typical DEW scatter correction and with mDEW scatter correction.

4. Discussion

The performance of our detector, as predicted by our MC simulations, competes with the results obtained with the VERITON CZT SPECT [5] for very similar exposures and activities, resolving the 6.4mm rods and with an equivalent image contrast. Nevertheless, our results still need to be validated by an experimental setup.

A very good performance is predicted for whole-body sizes although worse than our prediction with smaller objects like the brain, as expected. This shows that our gap and edge correction is still working well despite of the inevitable lager gaps. Further correction methods may be necessary for larger radius (i.e. imaging of larger objects).

The modified dual-energy window scatter correction shows promise for ^{99m}Tc, but more sophisticated methods will be necessary to account on low-energy tail in a multi-tracer imaging scenario. MC-based models could solve this issue [13, 21].

5. Conclusion

In this paper, we proposed an eight-head, swiveling, CZT SPECT detector with broad-energy collimators and showed its performance for whole-body imaging with body-sized phantoms. We improved our detector model with respect to [6] by combining the Geant4 MC simulation with a FEM for the CIE of the CZT detectors, which we showed is an important effect to take into account for our imaging purposes with a CZT camera. We can resolve 6.4mm features in a Derenzo phantom and obtain a CRC larger than 50% for features larger than 20mm.

In the future, we plan to validate our simulation framework with real data from a CZT camera prototype and to provide a proof of principle of imaging of ^{99m}Tc and other radionuclides (^{123}I, ^{177}Lu, etc.). This will provide demonstration of a system with excellent sensitivity and spatial resolution like the VERITON CZT SPECT, with the important addition of a broad energy range application, which would be very important for emerging new imaging radionuclides and for theranostics.

References

1. Van den Wyngaert, T., et al., *SPECT/CT: Standing on the Shoulders of Giants, It Is Time to Reach for the Sky!* Journal of Nuclear Medicine, 2020. **61**(9): p. 1284-1291.
2. Imbert, L., et al., *A one-shot whole-body bone SPECT may be recorded in less than 20 minutes with the high-sensitivity Veriton® CZT-camera.* Journal of Nuclear Medicine, 2019. **60**(supplement 1): p. 1288-1288.
3. Lee, J.S., et al., *Advances in imaging instrumentation for nuclear cardiology.* J Nucl Cardiol, 2019. **26**(2): p. 543-556.
4. Goshen, E., et al., *Feasibility study of a novel general purpose CZT-based digital SPECT camera: initial clinical results.* EJNMMI Phys, 2018. **5**(1): p. 6.
5. Desmonts, C., et al., *Evaluation of a new multipurpose whole-body CzT-based camera: comparison with a dual-head Anger camera and first clinical images.* EJNMMI Phys, 2020. **7**(1): p. 18.
6. Huh, Y., et al., *Evaluation of a variable-aperture full-ring SPECT system using large-area pixelated CZT modules: A simulation study for brain SPECT applications.* Medical Physics, 2021. **48**(5): p. 2301-2314.
7. Weng, F., et al., *An energy-optimized collimator design for a CZT-based SPECT camera.* Nucl Instrum Methods Phys Res A, 2016. **806**: p. 330-339.
8. Hirao, K., et al., *The prediction of rapid conversion to Alzheimer's disease in mild cognitive impairment using regional cerebral blood flow SPECT.* Neuroimage, 2005. **28**(4): p. 1014-1021.
9. Neumeyer, J.L., et al., *N-Omega-Fluoroalkyl Analogs of (1r)-2-Beta-Carbomethoxy-3-Beta-(4-Iodophenyl)-Tropane (Beta-Cit) - Radiotracers for Positron Emission Tomography and Single-Photon Emission Computed-Tomography Imaging of Dopamine Transporters.* Journal of Medicinal Chemistry, 1994. **37**(11): p. 1558-1561.
10. Myronakis, M.E. and D.G. Darambara, *Monte Carlo investigation of charge-transport effects on energy resolution and detection efficiency of pixelated CZT detectors for SPECT/PET applications.* Medical Physics, 2011. **38**(1): p. 455-467.

11. Mann, S. and M. Tornai, *Initial evaluation of a modified dual-energy window scatter correction method for CZT-based gamma cameras for breast SPECT.* SPIE Medical Imaging. Vol. 9413. 2015: SPIE.
12. Bolotnikov, A.E., et al., *Te Inclusions in CZT Detectors: New Method for Correcting Their Adverse Effects.* Ieee Transactions on Nuclear Science, 2010. **57**(2): p. 910-919.
13. Holstensson, M., et al., *Model-based correction for scatter and tailing effects in simultaneous 99mTc and 123I imaging for a CdZnTe cardiac SPECT camera.* Phys Med Biol, 2015. **60**(8): p. 3045-63.
14. Guerra, P., A. Santos, and D.G. Darambara, *Development of a simplified simulation model for performance characterization of a pixellated CdZnTe multimodality imaging system.* Physics in Medicine and Biology, 2008. **53**(4): p. 1099-1113.
15. Prettyman, T.H., *Method for mapping charge pulses in semiconductor radiation detectors.* Nuclear Instruments & Methods in Physics Research Section a-Accelerators Spectrometers Detectors and Associated Equipment, 1999. **422**(1-3): p. 232-237.
16. Prettyman, T.H., *Theoretical framework for mapping pulse shapes in semiconductor radiation detectors.* Nuclear Instruments & Methods in Physics Research Section a-Accelerators Spectrometers Detectors and Associated Equipment, 1999. **428**(1): p. 72-80.
17. Jan, S., et al., *GATE V6: a major enhancement of the GATE simulation platform enabling modelling of CT and radiotherapy.* Phys Med Biol, 2011. **56**(4): p. 881-901.
18. Barrett, H.H., J.D. Eskin, and H.B. Barber, *Charge transport in arrays of semiconductor gamma-ray detectors.* Phys Rev Lett, 1995. **75**(1): p. 156-159.
19. Jaszczak, R.J., et al., *Improved Spect Quantification Using Compensation for Scattered Photons.* Journal of Nuclear Medicine, 1984. **25**(8): p. 893-900.
20. Pourmoghaddas, A., et al., *Scatter correction improves concordance in SPECT MPI with a dedicated cardiac SPECT solid-state camera.* Journal of Nuclear Cardiology, 2015. **22**(2): p. 334-343.
21. Suzuki, A., et al., *Monte Carlo-based scatter correction considering the tailing effect of a CdTe detector for dual-isotope brain SPECT imaging.* Biomedical Physics & Engineering Express, 2016. **2**(4).
22. Shepp, L.A. and Y. Vardi, *Maximum likelihood reconstruction for emission tomography.* IEEE Trans Med Imaging, 1982. **1**(2): p. 113-22.
23. Thielemans, K., et al., *STIR: software for tomographic image reconstruction release 2.* Phys Med Biol, 2012. **57**(4): p. 867-83.
24. Fuster, B.M., et al., *Integration of advanced 3D SPECT modeling into the open-source STIR framework.* Medical physics, 2013. **40**(9): p. 092502.

Acknowledgments

This work was supported in part by National Institute of Biomedical Imaging and Bioengineering under grants R01EB026331 and R01EB012965, National Heart, Lung, and Blood Institute under grant R01HL135490.

Conflict of interest statement

The authors have no relevant conflicts of interest to disclose.